Symmetry-dependent transport properties and bipolar spin filtering in zigzag α-graphyne nanoribbons

Qu Yue, Shengli Chang, Jichun Tan, Shiqiao Qin, Jun Kang, and Jingbo Li

Symmetry-dependent transport properties and bipolar spin-filtering in zigzag α-graphyne nanoribbons

Qu Yue, Shengli Chang, Jichun Tan, and Shiqiao Qin
School of Science, National University of Defense Technology, Changsha 410073, China.

Jun Kang and Jingbo Li*
State Key Laboratory for Superlattice and Microstructures,
Institute of Semiconductors, Chinese Academy of Sciences, Beijing 100083, China.
(Dated: November 1, 2012)

First-principles calculations are performed to investigate the transport properties of zigzag α-graphyne nanoribbons (ZαGNRs). It is found that asymmetric ZαGNRs behave as conductors with linear current-voltage relationship, whereas symmetric ZαGNRs have very small currents under finite bias voltages, similar to those of zigzag graphene nanoribbons. The symmetry-dependent transport properties arise from different coupling rules between the π and π^* subbands around the Fermi level, which are dependent on the wavefunction symmetry of the two subbands. Based on the coupling rules, we further demonstrate the bipolar spin-filtering effect in the symmetric ZαGNRs. It is shown that nearly 100% spin-polarized current can be produced and modulated by the direction of bias voltage and/or magnetization configuration of the electrodes. Moreover, the magnetoresistance effect with the order larger than 500,000% is also predicted. Our calculations suggest ZαGNRs as one of promising candidate materials for novel spintronics.

I. INTRODUCTION

Graphene, a single layer of sp^2 hybridized carbon atoms in a honeycomb lattice, has been extensively studied for application in the next-generation nanodevices because of its outstanding properties[1–4]. In particular, zigzag graphene nanoribbon (ZGNR) has attracted research interest as a hopeful candidate material for spintronics devices, owing to its magnetic zigzag edges[5,6] and unique transport properties[7,8]. So far, a number of theoretical schemes have been proposed in this direction. For example, it is shown that ZGNR becomes half-metal by applying external electric field[2,9] or chemical modification[10–12], which can be utilized for generation of spin polarized current. Also, bipolar spin-filtering and larger magnetoresistance (MR) effects have been predicted in a ZGNR-based spin-valve device, in which ZGNR is connected to two electrodes and external magnetic fields are applied to these electrodes with different magnetization configurations[13–16]. Meanwhile, graphene-based spin devices have been constructed experimentally[17–19]. Tombros et $al.$ demonstrated the spin injection in graphene via a cobalt electrode at room temperature and detected the up-spin and down-spin currents by using a nonlocal measurement method[17]. Recently, Bai et $al.$ observed a negative magnetoresistance of nearly 100% at low temperature in graphene nanoribbons[18].

Besides graphene, graphyne, a new allotrope of carbon containing sp and sp^2 hybridized carbon atoms, has also been the subject of interest[20–30]. Due to the presence of acetylenic bonds in the structure, graphyne is thought to have rich electronic and optical properties that are different from those of graphene[31]. Indeed, it has been found that graphyne is semiconductor with a narrow gap[21]. Nevertheless, recently Malko et $al.$ found that α-graphyne and other graphyne derivatives can behave as gapless semiconductor similar to graphene[32,33], which extends the application scope of graphyne in nanoelectronics and photoelectronics. Then a question of fundamental interest is whether the spin-filtering and MR effects can be actualized in α-graphyne similar to or even more fascinating than those of graphene. In this paper, we focus our attention on the zigzag α-graphyne nanoribbons (ZαGNRs). From the first-principles calculations, we initially explore the transport properties of ZαGNRs, and show that the ZαGNRs with symmetric and asymmetric structures exhibit different transport behaviors. Then, based on this symmetry-dependent transport behavior, we demonstrate the bipolar spin-filtering and magnetoresistance effects in the symmetric ZαGNRs-based device. Our works suggest a new route to manipulate spin current and design the spintronic devices for complementing the graphene-based spin devices. What's more, it will put a urgency on the experimental study of graphyne as well.

II. METHODS

Electronic structures are calculated within the density functional theory (DFT) by using the SIESTA code[34]. The generalized gradient approximation (GGA) with Perdew-Burke-Ernzerhof (PBE) functional[35] is employed for the exchange-correction potential and norm-conserving Troullier-Martins pseudopotentials[36] are used for the core-valence interactions. The single-ζ polarized numerical atomic-orbital basis sets for C and H are adopted. The cutoff is set to be 300 Ry for real-space grid. A vacuum layer larger than 10 Å is used to avoid interaction between adjacent ribbons. The energy level is populated using the Fermi-Dirac distribution ($k_B T$=25 meV). All atomic positions are fully relaxed until the Hellmann-Feynman force on each atom is less than 0.04 eV/Å. The transport properties are studied by using nonequilibrium Green's function method, as implemented in the TranSIESTA module[37]. The spin-polarized current through the system is calculated using Landauer-Büttiker formula[38],

$$I_\sigma(V_\mathrm{b}) = \frac{e}{h} \int_{-\infty}^{\infty} \{T_\sigma(E, V_\mathrm{b})[f_\mathrm{L}(E, V_\mathrm{b}) - f_\mathrm{R}(E, V_\mathrm{b})]\} dE \tag{1}$$

where e is the electron charge, h is the Planck's constant, and T_σ is the transmission value of an electron with spin σ. $f_\mathrm{L(R)}(E, V_\mathrm{b}) = n_\mathrm{F}(E - \mu_\mathrm{L(R)})$, n_F and $\mu_\mathrm{L(R)}$ are the Fermi distribution function and the chemical potentials of left and right electrodes, respectively. T_σ is obtained from the equation

$$T_\sigma(E, V_\mathrm{b}) = Tr[\mathrm{Im}\{\Sigma_\mathrm{L\sigma}^r(E, V_\mathrm{b})\} G_\sigma^r(E, V_\mathrm{b}) \times \mathrm{Im}\{\Sigma_\mathrm{R\sigma}^r(E, V_\mathrm{b})\} G_\sigma^a(E, V_\mathrm{b})] \tag{2}$$

where G^r (G^a) is the retarded (advanced) Green's function matrix, and Σ_L^r (Σ_R^r) is the retarded self-energy matrix for the left (right) electrode. Also, it is straightfoward to extend the equations for the spin-unpolarized case.

III. RESULTS AND DISCUSSION

The ZαGNRs are originally obtained by cutting a 2D α-graphyne along zigzag lines, and the edges are passivated by single H atoms to remove the dangling bonds. Following conventional custom, the widths can be characterized by the number of zigzag C chains along the nanoribbon axis, namely, N-ZαGNRs. Considering the symmetry, the
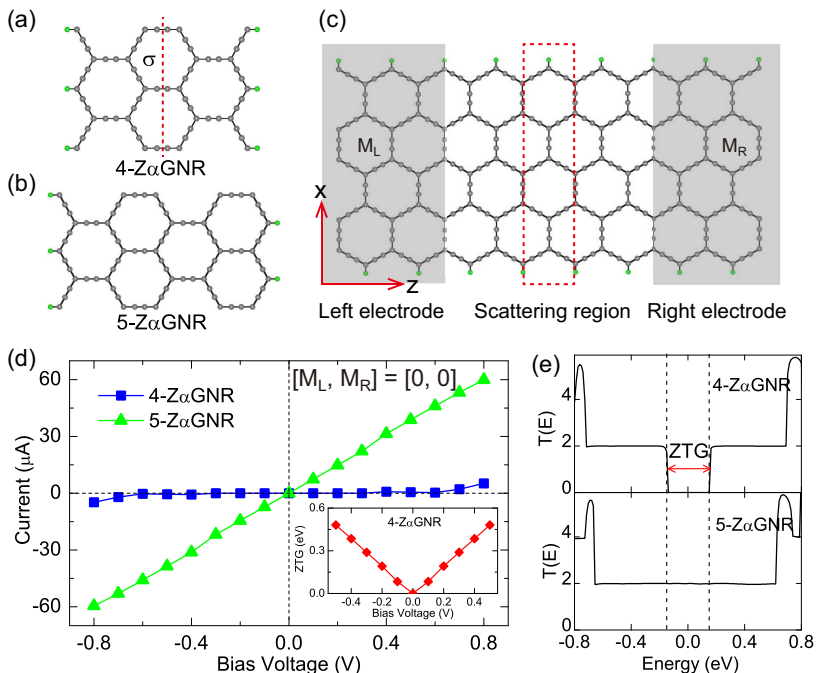
FIG. 1. Geometric structures of (a) 4-ZαGNR and (b) 5-ZαGNR. Gray and green balls correspond to C and H atoms, respectively. The red dashed line denotes the mirror plane σ. (c) Schematic structure of the two probe system. Red dashed rectangle indicates the primitive unit cell of ZαGNR. M_L and M_R represent the magnetization of left and right electrodes under the magnetic field, respectively. (d) The variation of current as a function of bias voltage. The zero transmission gap versus bias for the 4-ZαGNR is given in the inset. (e) Transmission spectra for 4-ZαGNR (upper) and 5-ZαGNR (lower) under 0.3 V. The vertical dashed lines denote the chemical potentials of left and right electrodes.

N-ZαGNRs are divided into two types, symmetric and asymmetric ZαGNRs, which correspond to even and odd N respectively.

A. Symmetry-dependent transport properties

Our previous work has shown that all the ZαGNRs have two types of spin states, ferromagnetic state and antiferromagnetic state, with the latter energetically preferred as the ground state[39]. The ferromagnetic ZαGNRs are metallic, whereas antiferromagnetic ones exhibit semiconducting behavior. The energy difference between the two spin states would decrease as the nanoribbon width increases. It seems that both symmetric and asymmetric ZαGNRs exhibit symmetry-independent magnetic and electronic properties. However, the results may be different with respect to the transport properties. It has been found that zigzag graphene nanoribbons have different transport behaviors under bias voltages, depending on the symmetry of the nanoribbons[7,40]. We wonder whether the ZαGNRs would possess similarly symmetry-dependent transport properties as the zigzag graphene nanoribbons do.

Here, we choose the 4-ZαGNR and 5-ZαGNR to represent the symmetric and asymmetric ZαGNRs, as shown in Figs. 1(a) and 1(b). Clearly, symmetric ribbons hold a mirror plane σ between the two edges, while the σ plane is absent in asymmetric ribbons. In order to examine the transport behaviors, we construct the two probe systems [Fig. 1(c)] based on both the 4- and 5-ZαGNRs. The systems consist of three portions, two semi-infinite electrodes and a scattering region. M_L and M_R represent the magnetization of the left and right electrodes, which can be controlled by external magnetic field[15,19]. M_L and M_R can be 1, 0, or -1, corresponding to magnetization along the $+y$ direction, non-magnetization, and magnetization along the $-y$ direction, respectively. The scattering region contains four primitive unit cells, with the length of 28.48 Å. And then we study the spin-unpolarized transport behaviors of the ZαGNRs, namely, $[M_L, M_R]=[0, 0]$. The calculated current (I) versus the bias voltage (V_b) is given in Fig. 1(d). Similar to the zigzag graphene nanoribbons, the transport behaviors of ZαGNRs are dependent on the symmetry of ribbons. For 5-ZαGNR, the current increases with increasing $|V_b|$ and obeys a linear relationship. It is attributed to the constant conductance of $2G_0$ within the applied voltage range. In contrast, the current of 4-ZαGNR is close to zero under finite bias, and begins to increase when the bias is stronger than a critical bias voltage (V_c).

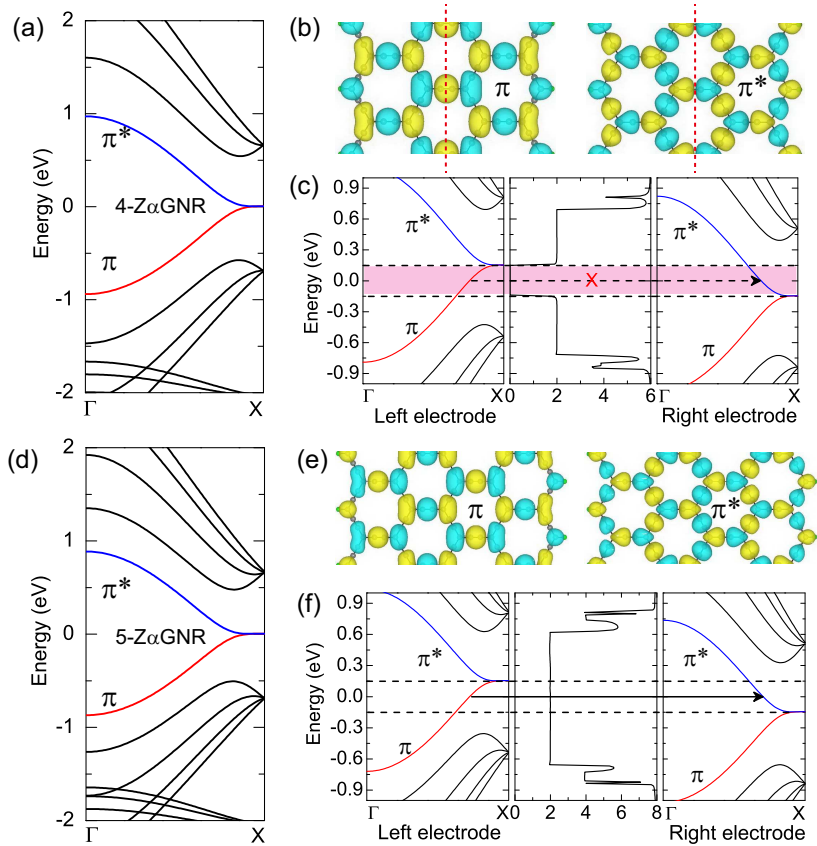FIG. 2. (a) Band structure of 4-ZαGNR. (b) Γ-point wavefunctions of π and π^* subbands for 4-ZαGNR. The yellow and blue colors indicate positive and negative signs, respectively. Red dashed lines denote the mirror plane. (c) Band structures for the left and right electrodes, and transmission spectrum for 4-ZαGNR under 0.3 bias voltage. (d)-(f) The same caption as (a)-(c) but for 5-ZαGNR. The pink shade in (c) indicates the ZTG for 4-ZαGNR, and the dashed arrow means the electron transmission is forbidden. The solid arrow in (f) means the transmission is allowed. The horizontal dashed lines in (c) and (f) denote the chemical potentials of left and right electrodes.

This current variation can be understood by the corresponding transmission spectrum. As shown in Fig. 1(e), a zero transmission gap (ZTG) appears around the Fermi level upon the bias is applied. Herein, the vertical dashed lines indicate the chemical potentials of left and right electrodes (μ_L and μ_R) separated by $e|V_b|$. The region between μ_L and μ_R is referred to as bias window. Moreover, the ZTG linearly increases with increasing bias voltage [The inset of Fig. 1(d)]. Because the ZTG is almost equal to the bias window between the chemical potentials of left and right electrodes, the transmission nearly keeps zero in the whole bias window. Consequently, the current of 4-ZαGNR remains small until the bias reaches V_c. Our results therefore demonstrate that ZαGNRs exhibit symmetry-dependent transport properties.

Next, we investigate the basic mechanism underlying the symmetry-dependent transport behaviors in ZαGNRs. Generally, the distinct transport properties should arise from the characteristics of band structures of 4- and 5-ZαGNRs, as shown in Figs. 2(a) and 2(d). However, it seems both of them exhibit very similar characteristics. Around the Fermi level, there exists two subbands, which meet near the X-point in the Brillouin zone. Based on the projected densities of states of 4- and 5-ZαGNRs [not shown here], it is found that states ranging from -2 to 3 eV origin from C $2p_z$ state. The two subbands around the Fermi level, accordingly, are bonding π and antibonding π^* bands. Thus, we can expect that the characteristics of π and π^* would determine the transport properties of ZαGNRs under small bias voltage. We now turn to the nature of wavefunctions of π and π^* subbands for 4- and 5-ZαGNRs, as plotted in Figs. 2(b) and 2(e). It is found that their wavefunctions do have different characteristics. The π (π^*) subband of 4-ZαGNR has even (odd) parity under the σ mirror operation, while the π (π^*) subband of 5-ZαGNR has no definite parity due to the absence of the mirror plane. Fig. 2(c) then shows the band structures of left and right electrodes and transmission spectrum for 4-ZαGNR under 0.3 V bias voltage. Within the bias window, only the π subband of left electrode overlaps with the π^* subband of right electrode. Since the π and π^* subbands have opposite parities with respect to the σ mirror operation, the electron transmission from the π subband of left electrode to

the π^* subband of right electrode is forbidden. As a result, ZTG appears around the Fermi level and no electron transmission contributes to the current. For 5-ZαGNR, the subband overlap between the two electrodes is similar to 4-ZαGNR in the bias window. However, as its π and π^* subbands have no definite parity, the electron transmission from the π subband of left electrode to the π^* subband of right electrode is allowed, leading to a $2G_0$ conductance and linear current-voltage characteristic as shown in Fig. 1(d).

B. Bipolar spin-filtering effect

Now we focus on the spin-polarized transport properties of symmetric ZαGNR by using the two probe system based on the 4-ZαGNR. Two magnetic configurations [M_L, M_R]=[1, 1] and [1, -1] are considered first. In the former configuration, both of the left and right electrodes are up-spin polarized, whereas the left electrode is up-spin polarized and the right one is down-spin polarized in the latter configuration. Their spin polarization directions are also confirmed by the spin densities under zero bias [Figs. 3(a) and 3(c)]. For the [1, -1] configuration, a more rigorous scheme involving noncollinear spin-polarization configuration would need to be considered. Previous studies have shown that, in the case of graphene nanoribbons, noncollinear spin polarization has only a minor influence on the transmission spectrum, and whether including or excluding this effect does not change the main results[15,41]. Since α-graphyne shows similar properties as graphene, it can be expected that the noncollinear spin effect on the ZαGNR is also small, and neglecting this effect would be reasonable. Thus, we still utilize the collinear spin configuration in our calculations. When the bias voltages are applied, the spin currents are obtained, as shown in Figs. 3(b) and 3(d). Obviously, the $I - V_b$ curves for the two configurations exhibit different characteristics. For [1, 1] configuration, the up-spin current $|I_{up}|$ increases rapidly with increasing $|V_b|$ under a low positive or negative bias, and then it nearly saturates with several μA when $|V_b|$ is larger than 0.2 V. The variation of down-spin current $|I_{down}|$ with $|V_b|$ are similar to the up-spin case. For [1, -1] configuration, the up-spin current I_{up} shows metallic behavior in the positive region of V_b, while it is completely suppressed in the negative region. On the other hand, the down-spin current I_{down} shows metallic behavior in the negative region of V_b, while it is completely suppressed in the positive region. The ratio of up-spin (down-spin) current to the total current increase gradually to over 99.9% (nearly 100 %) as V_b increases to 0.2 V (-0.2 V) [Fig. 3(e)]. Consequently, a perfect bipolar spin-filtering effect is observed. It seems that these $I - V_b$ characteristics depend on not only the spin, but also the direction of bias voltage.

The spin-filtering effect can be understood by examining the V_b dependence of the transmission spectrum in [1, -1] configuration. As shown in Fig. 3(f), there exists a ZTG of 0.36 eV for both the up-spin and down-spin states around the Fermi level under zero bias, and the current is zero. Upon the application of bias, the ZTG is found to vary as a function of V_b. For up-spin state, when V_b is below 0.2 V, ZTG linearly decreases with increasing V_b. However, because the ZTG is still larger than the bias window, I_{up} remains zero. Then, ZTG for up-spin state continually decreases with increasing V_b and reaches 0 when $0.35 \leq V_b \leq 0.40$ V. Within this range, ZTG becomes smaller than the bias window, the electron transmission contributes to the current flow, and I_{up} starts to increase. Once V_b is larger than 0.4 V, zero transmission gap appears again and I_{up} almost saturates. The variation of ZTG for up-spin state is different as V_b increases towards the negative direction. ZTG first increases with increasing V_b and reaches the maximum of 0.73 eV at -0.4 V, beyond which ZTG starts to decrease. Since ZTG is always larger than the bias window in the negative region of V_b, I_{up} is completely blocked. In contrast, the variation of ZTG for down-spin state is totally opposite to that for up-spin state in the positive region of V_b, as well as the negative region.

The increasing and decreasing of ZTG are attributed to the band structures of the left and right electrodes of 4-ZαGNR. At $V_b = 0$ V [Fig. 4(a)], near the Fermi level the up-spin π^* subband of left electrode only overlaps with the up-spin π subband of right electrode. As the π and π^* subbands have opposite parities under the σ mirror operation, the electron transmission between them is hence forbidden, resulting in a gap of 0.36 eV (yellow shade region). When V_b increases to 0.2 V [Fig. 4(b)], the energy region where the up-spin π^* subband of left electrode only overlaps with up-spin π subband of right electrode decreases, and contributes to a 0.16 eV gap, which is slightly smaller than the bias window (0.2 V). Then, when V_b reaches the range from 0.35 to 0.4 V [Fig. 4(c)], the up-spin π subbands, as well as the up-spin π^* subbands, of the two electrodes overlap, respectively. As a result, the electron transmission within the bias window is completely allowed and the ZTG disappears. Fig. 4(d) plots the band structures for $V_b = 0.5$ V case. Near the Fermi level, the up-spin π subband of left electrode only overlaps the up-spin π^* of right electrode. Due to the absent of transmission between the two subbands, a gap of 0.08 eV opens again. On the other hand, for the down-spin state the π subband of left electrode only overlaps with the π^* subband of right electrode around the Fermi level, as V_b increases towards the positive direction. Therefore, the gap remains open owing to the parity mismatch of the spin-down subbands [Figs. 4(a)-4(d)]. The above analysis can also apply to the case when V_b increases towards the negative direction.

Apart from the [1, 1] and [1, -1] magnetic configurations, we also investigate the spin-polarized transport properties of 4-ZαGNR with [0, 1] and [0, -1] configurations. 0 represents the nonmagnetic state of left electrode and ± 1
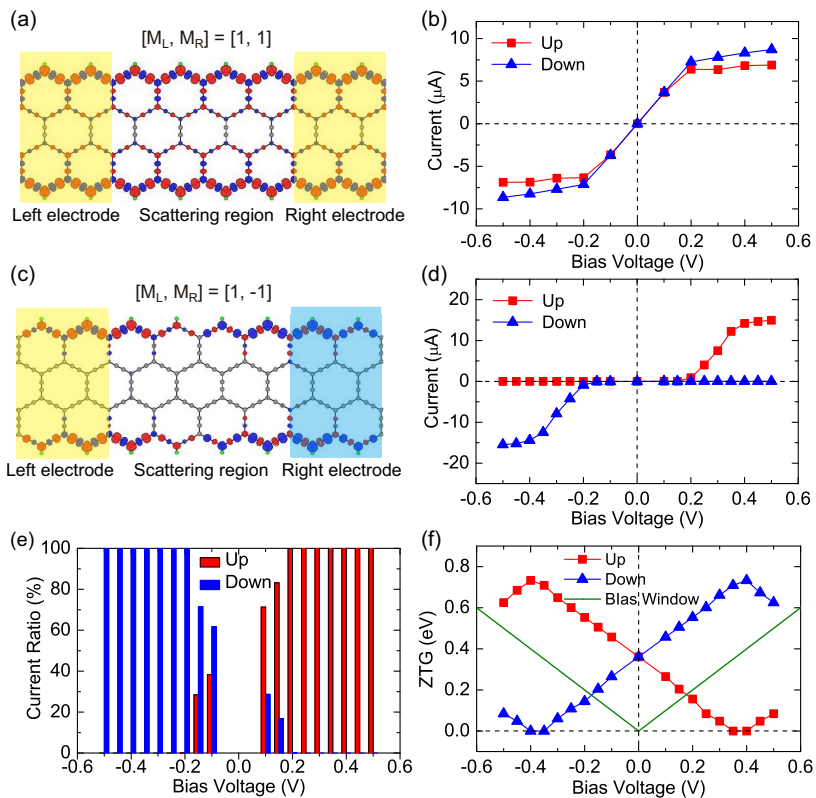
FIG. 3. (a) Spin density for 4-ZαGNR with $[M_L, M_R]$=[1, 1] configuration under zero bias. The red and blue colors stand for the up-spin and down-spin components, respectively. The isosurface level is taken as 0.006 $e/\text{Å}^3$. (b) The $I - V_b$ curve for 4-ZαGNR with [1, 1] configuration. (c)-(d) The same information as (a)-(b) but for 4-ZαGNR with $[M_L, M_R]$=[1, -1] configuration. (e) The ratio of each spin current to the total current versus the bias voltage. Red and blue bars correspond to the up-spin and down-spin components. (f) ZTG versus bias for 4-ZαGNR with [1, -1] configuration. The green solid lines indicates the value of bias window. In (b), (d) and (f), the up-spin and down-spin currents are denoted by red square and blue triangle symbols.

represents the magnetization of right electrode. The variation of spin current with bias is shown in Figs. 5(a) and 5(b). Obviously, the bipolar spin-filtering behavior is also obtained in the two configuration analogous to that in [1, -1] configuration. It is found that the ratio of up-spin (down-spin) current to the total current rapidly increases to nearly 100% at very low bias, which indicates that very low working voltage is required to operate such system. Based on the same magnetic configuration, zeng *et al.*[13] demonstrated similar spin-filtering behavior in zigzag graphene nanoribbons. Nonetheless, it is found that there exists a small leakage current in the cutoff region, and thus the ratio of each spin to the total current is lower than that of ZαGNRs. This spin-filtering effect can be simply understood from the band structures of left and right electrodes plotted in Figs. 5(c) and 5(d) for the [0, 1] configuration. At zero bias, near the Fermi level the up-spin π (down-spin π^*) subband of left electrode only overlaps with the up-spin π^* (down-spin π) subband of right electrode, the transmission is forbidden owing to the opposite parities between the two subbands, the ZTG thus appears for both spin components. When V_b reaches 0.2 V, the situation becomes different. Within the bias window, the up-spin π subband of left electrode only overlaps with the up-spin π^* subband of right electrode, the electron transmission is forbidden and I_{up} keeps zero. In contrast, both the down-spin π subbands of left and right electrodes overlap, and the transmission is allowed, leading to a down-spin current flow.

It is shown that combining spin transport properties and magnetization direction of electrons can give rise to the MR effect in zigzag graphene nanoribbons[15]. Here, based on the different transport behaviors of 4-ZαGNR with [1, 1] and [1, -1] configurations, the MR effect can also be realized. As shown in Fig. 3(d), for [1, -1] configuration, the spin current is quiet small within the bias range $-0.15 < V_b < 0.15$ V, indicating a very high differential resistance. For [1, 1] configuration, the spin current increases rapidly and remains linear when $-0.15 < V_b < 0.15$ V, indicating a relatively low differential resistance [Fig. 3(b)]. According to the definition[42], $MR = (I_{1,1} - I_{1,-1})/I_{1,-1}$, where $I_{1,-1}$ and $I_{1,1}$ are the spin current in the [1, 1] and [1, -1] configuration, respectively. The calculated MR value is given in Fig. 6. It is found that the system shows very stronger MR effect, and the up-spin, down-spin and total MRs are all larger than 500,000%.
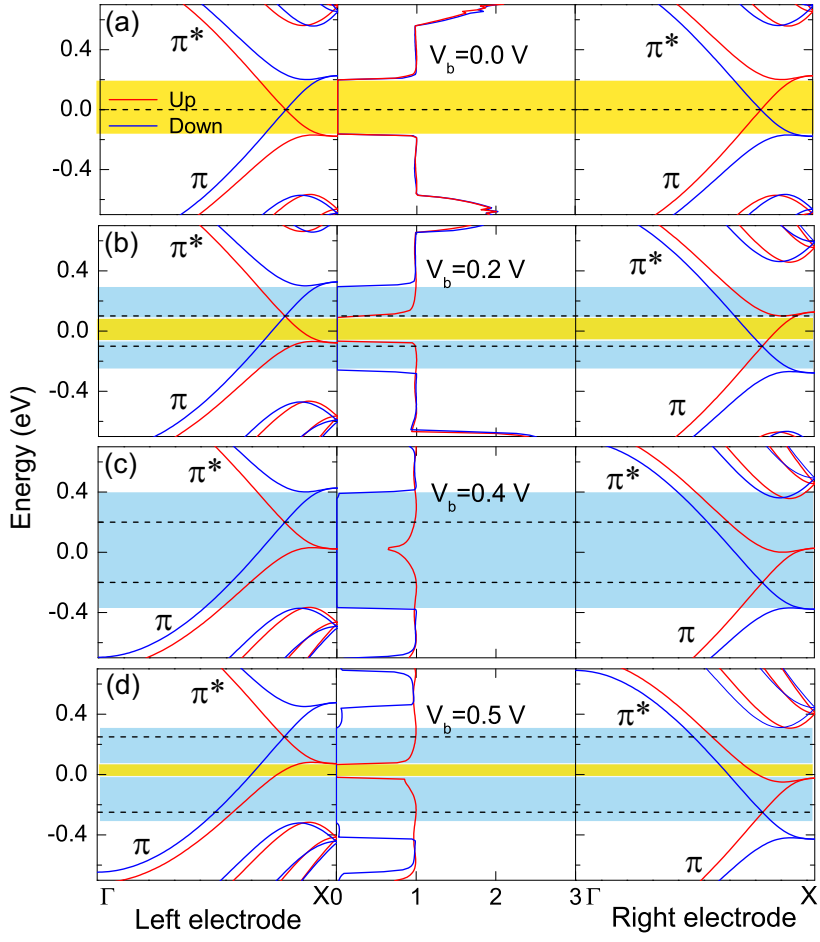
FIG. 4. Band structure for the left electrode (left panel), transmission spectrum (middle panel), and band structure for the right electrode (right panel) for 4-ZαGNR with [1, -1] configuration. (a)-(d) correspond to 0.0, 0.2, 0.4 and 0.5 V bias cases, respectively. The yellow and blue shades show the ZTG for the up-spin and down-spin states. The horizontal dashed lines denote the chemical potentials of left and right electrodes.

IV. SUMMARY

In summary, we investigate the transport properties of ZαGNRs using the first-principles calculations. It is found that ZαGDNRs exhibit symmetry-dependent transport characteristics which arise from the different wavefunctions symmetry of π and π^* subbands near the Fermi level for symmetric and asymmetric ZαGDNRs. While symmetric ZαGNRs have very small currents in the presence of a ZTG around the Fermi level, asymmetric ZαGNRs behave as conductors with two conductance quantum. And then, we demonstrate the bipolar spin filter effect in a two-terminal device constructed by symmetry ZαGNR. It is shown that the behaviors of spin-up and spin-down currents depend on not only the direction of bias voltage, but also the magnetization configuration of the electrodes. Besides, MR effect with the order larger than 500,000% is predicted. Our results show that the ZαGNRs hold promise for developing ideal spin-valve device in future spintronics.
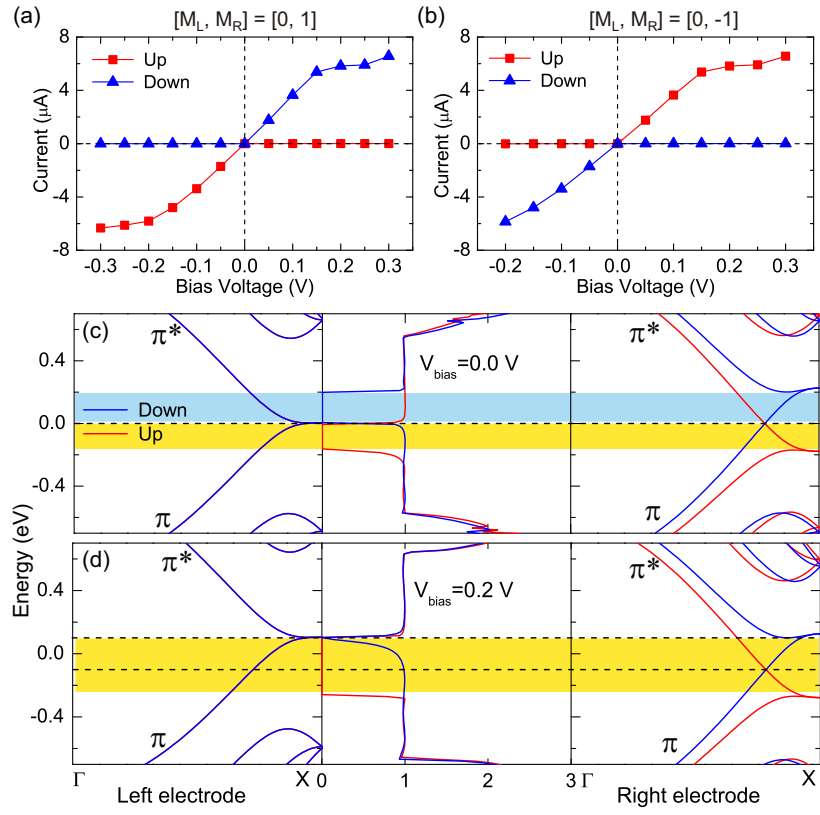
FIG. 5. The $I - V_b$ curve for 4-ZαGNR with (a) $[M_L, M_R]$=[0, 1] and (b) $[M_L, M_R]$=[0, -1] configurations. Red square and blue triangle symbols denote the up-spin and down-spin currents, respectively. Band structure for the left electrode (left panel), transmission spectrum (middle panel), and band structure for the right electrode (right panel) for 4-ZαGNR with [0, 1] configuration under (c) 0.0, and (d) 0.2 V bias voltage. The up-spin and down-spin states are degenerate in all energy bands of left electrode. The yellow and blue shades show the ZTG for the up-spin and down-spin states, respectively. The horizontal dashed lines denote the chemical potentials of left and right electrodes.
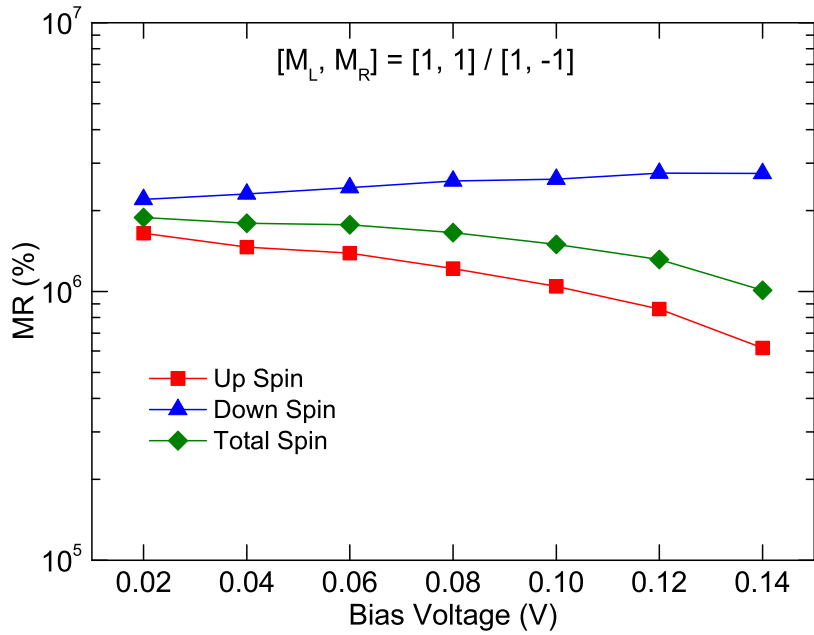

FIG. 6. Log-scale of the up-spin, down spin and total magnetoresistance versus the bias voltage. Red square, blue triangle and green diamond symbols correspond to the up-spin, down-spin and total spin cases.

* jbli@semi.ac.cn

[1] K. S. Novoselov, A. K. Geim, S. V. Morozov, D. Jiang, Y. Zhang, S. V. Dubonos, I. V. Grigorieva, and A. A. Firsov, Science **306**, 666–669 (2004).

[2] Y.-W. Son, M. L. Cohen, and S. G. Louie, Nature **444**, 347–349 (2006).

[3] C. Józsa, M. Popinciuc, N. Tombros, H. T. Jonkman, and B. J. van Wees, Phys. Rev. Lett. **100**, 236603 (2008).

[4] S. K. Min, W. Y. Kim, Y. Cho, and K. S. Kim, Nature Nanotechnol. **6**, 162–165 (2011).

[5] O. V. Yazyev and M. I. Katsnelson, Phys. Rev. Lett. **100**, 047209 (2008).

[6] L. Pisani, J. A. Chan, B. Montanari, and N. M. Harrison, Phys. Rev. B **75**, 064418 (2007).

[7] Z. Li, H. Qian, J. Wu, B.-L. Gu, and W. Duan, Phys. Rev. Lett. **100**, 206802 (2008).

[8] Q. Yan, B. Huang, J. Yu, F. Zheng, J. Zang, J. Wu, B.-L. Gu, F. Liu, and W. Duan, Nano Lett. **7**, 1469–1473 (2007).

[9] E.-J. Kan, Z. Li, J. Yang, and J. G. Hou, Applied Physics Letters **91**, 243116 (2007).

[10] M. Wu, X. Wu, Y. Gao, and X. C. Zeng, Applied Physics Letters **94**, 223111 (2009).

[11] S. Dutta, A. K. Manna, and S. K. Pati, Phys. Rev. Lett. **102**, 096601 (2009).

[12] E.-J. Kan, Z. Li, J. Yang, and J. G. Hou, J. Am. Chem. Soc. **130**, 4224–4225 (2008).

[13] M. Zeng, L. Shen, M. Zhou, C. Zhang, and Y. Feng, Phys. Rev. B **83**, 115427 (2011).

[14] T. Ozaki, K. Nishio, H. Weng, and H. Kino, Phys. Rev. B **81**, 075422 (2010).

[15] W. Y. Kim and K. S. Kim, Nature Nanotechnol. **3**, 408–412 (2008).

[16] R. Qin, J. Lu, L. Lai, J. Zhou, H. Li, Q. Liu, G. Luo, L. Zhao, Z. Gao, W. N. Mei, and G. Li, Phys. Rev. B **81**, 233403 (2010).

[17] N. Tombros, C. Jozsa, M. Popinciuc, H. T. Jonkman, and B. J. van Wees, Nature **448**, 571–574 (2007).

[18] J. Bai, R. Cheng, F. Xiu, L. Liao, M. Wang, A. Shailos, K. L. Wang, Y. Huang, and X. Duan, Nature Nanotechnol. **5**, 655–659 (2010).

[19] W. H. Wang, K. Pi, Y. Li, Y. F. Chiang, P. Wei, J. Shi, and R. K. Kawakami, Phys. Rev. B **77**, 020402 (2008).

[20] R. H. Baughman, H. Eckhardt, and M. Kertesz, J. Chem. Phys. **87**, 6687–6699 (1987).

[21] N. Narita, S. Nagai, S. Suzuki, and K. Nakao, Phys. Rev. B **58**, 11009–11014 (1998).

[22] M. Long, L. Tang, D. Wang, Y. Li, and Z. Shuai, ACS Nano **5**, 2593–2600 (2011).

[23] Q. Zheng, G. Luo, Q. Liu, R. Quhe, J. Zheng, K. Tang, Z. Gao, S. Nagase, and J. Lu, Nanoscale **4**, 3990–3996 (2012).

[24] J. Kang, J. Li, F. Wu, S.-S. Li, and J.-B. Xia, J. Phys. Chem. C **115**, 20466–20470 (2011).

[25] V. R. Coluci, S. F. Braga, S. B. Legoas, D. S. Galvão, and R. H. Baughman, Phys. Rev. B **68**, 035430 (2003).

[26] G. Luo, X. Qian, H. Liu, R. Qin, J. Zhou, L. Li, Z. Gao, E. Wang, W.-N. Mei, J. Lu, Y. Li, and S. Nagase, Phys. Rev. B **84**, 075439 (2011).

[27] K. Srinivasu and S. K. Ghosh, J. Phys. Chem. C **116**, 5951–5956 (2012).

[28] L. D. Pan, L. Z. Zhang, B. Q. Song, S. X. Du, and H.-J. Gao, Applied Physics Letters **98**, 173102 (2011).

[29] Y. Jiao, A. Du, M. Hankel, Z. Zhu, V. Rudolph, and S. C. Smith, Chem. Commun. **47**, 11843–11845 (2011).

[30] Y. Guo, K. Jiang, B. Xu, Y. Xia, J. Yin, and Z. Liu, J. Phys. Chem. C **116**, 13837–13841 (2012).

[31] S. W. Cranford and M. J. Buehler, Carbon **49**, 4111 – 4121 (2011).

[32] D. Malko, C. Neiss, F. Viñes, and A. Görling, Phys. Rev. Lett. **108**, 086804 (2012).

[33] D. Malko, C. Neiss, and A. Görling, Phys. Rev. B **86**, 045443 (2012).

[34] J. Soler, E. Artacho, J. Gale, A. Garcia, J. Junquera, P. Ordejon, and D. Sanchez-Portal, J. Phys.: Condens. Matter **14**, 2745–2779 (2002).

[35] J. P. Perdew, K. Burke, and M. Ernzerhof, Phys. Rev. Lett. **77**, 3865–3868 (1996).

[36] N. Troullier and J. Martins, Solid State Commun. **74**, 613 – 616 (1990).

[37] M. Brandbyge, J.-L. Mozos, P. Ordejón, J. Taylor, and K. Stokbro, Phys. Rev. B **65**, 165401 (2002).

[38] S. Datta, *Electronic Transport in Mesoscopic Systems* (Cambridge University Press, 1995).

[39] Q. Yue, S. Chang, J. Kang, J. Tan, S. Qin, and J. Li, J. Chem. Phys. **136**, 244702 (2012).

[40] W. Y. Kim, Y. C. Choi, S. K. Min, Y. Cho, and K. S. Kim, Chem. Soc. Rev. **38**, 2319–2333 (2009).

[41] W. Y. Kim and K. S. Kim, Acc. Chem. Res. **43**, 111–120 (2010).

[42] J. Kang, F. Wu, and J. Li, Appl. Phys. Lett. **100**, 233122 (2012).